

EFFECTIVE PERMEABILITIES FOR FLOW THROUGH ANISOTROPIC MICROSCOPIC GEOMETRIES

L. BALAZI*, F. HOLZBERGER[§], S. B. LUNOWA[§], M. A. PETER[†], D. PETERSEIM[†], B. WOHLMUTH[§]

ABSTRACT. This work develops a computational and theoretical framework for determining effective permeabilities in anisotropic microscopic geometries containing dense, fibre-like obstacles, motivated by the need to model flow in coiled aneurysm domains accurately. Building on homogenisation theory and fully resolved simulations in Representative Elementary Volumes (REVs), we validate the permeability model introduced in [C. Boutin, Study of permeability by periodic and self-consistent homogenisation. Eur. J. Mech. A Solids, 19(4):603–632, 2000] and propose a systematic methodology for capturing the directional variations induced by fibre orientation. The resulting permeability tensors are incorporated into macroscopic flow simulations based on the Darcy equation, enabling direct comparison of anisotropic and isotropic permeability models across several benchmark configurations.

Our findings show that anisotropy has a significant impact on local flow direction and magnitude, generating directional permeability contrasts which cannot be reproduced by classical isotropic approximations. By integrating coil-induced microstructural effects into continuum-scale hemodynamic models, the proposed approach enables more realistic assessment of post-treatment aneurysm flow behaviour. Beyond this clinical application, the framework is broadly applicable to other biomedical and engineering systems involving fibrous or filamentous porous microstructures.

Key words. Effective permeability, Anisotropic microstructures, Homogenisation, Darcy equation, Coiled aneurysms

AMS subject classifications. 76M50, 35B27, 76Z05, 92C35, 92C50

1. INTRODUCTION

The precise computation of flow through porous media is essential for many engineering applications, such as groundwater transport through soil [5]. In this work, we consider the underlying concepts in the context of a medical application, that is blood flow through thin wired devices such as endovascular coils. Endovascular coiling is one of the common treatment methods for cerebral aneurysms. Understanding and predicting the flow through such coils is of high current interest [1, 16].

A cerebral aneurysm is a saccular malformation of a brain artery, which develops due to the gradual dilation of the vessel wall over time. The primary health danger lies in the fact that the artery walls become progressively thinner and weaker, up to the point where they can rupture even under relatively low stresses. In this case, a subarachnoid haemorrhage occurs, leading to blood entering the subarachnoid space. The sudden increase in intracranial pressure and disturbance of the normal circulation of the cerebrospinal fluid can lead to severe brain

* INSTITUTE OF MATHEMATICS, UNIVERSITY OF AUGSBURG, UNIVERSITÄTSSTR. 12A, 86159 AUGSBURG, GERMANY

[§] DEPARTMENT OF MATHEMATICS, SCHOOL OF COMPUTATION, INFORMATION AND TECHNOLOGY, TECHNICAL UNIVERSITY OF MUNICH, 85748 GARCHING B. MÜNCHEN, GERMANY

[†] INSTITUTE OF MATHEMATICS & CENTRE FOR ADVANCED ANALYTICS AND PREDICTIVE SCIENCES (CAAPS), UNIVERSITY OF AUGSBURG, UNIVERSITÄTSSTR. 12A, 86159 AUGSBURG, GERMANY

E-mail address: loic.balazi@uni-a.de, malte.peter@uni-a.de, daniel.peterseim@uni-a.de, fabian.holzberger@tum.de, stephan.lunowa@tum.de, wohlmuth@cit.tum.de.

Date: December 5, 2025.

F. Holzberger, S. B. Lunowa and B. Wohlmuth gratefully acknowledge the financial support provided by the German Research Foundation (Deutsche Forschungsgemeinschaft, DOI 10.13039/501100001659) under project number 465242983 within the priority programme “SPP 2311: Robust coupling of continuum-biomechanical in silico models to establish active biological system models for later use in clinical applications – Co-design of modeling, numerics and usability”.

L. Balazi, M. A. Peter and D. Peterseim gratefully acknowledge the support of the Centre for Future Production of University of Augsburg.

damage and death. Fortunately, treatments have been rapidly progressing in the last decades and for a large amount of patients a minimally invasive procedure can be applied. Among these, endovascular coiling involves the insertion of thin metallic wires, through a micro catheter, into the aneurysm, which then coil up, creating a form of plug. This procedure directly occludes the aneurysm from the blood flow, lowering the chance of rupture due to sudden haemodynamic changes and is often even applied when rupture has already occurred. What is more, the presence of the metallic coils further promotes blood clotting within the aneurysm sac, leading to even better occlusion and, in the best case, to the gradual healing and reconstruction of the vessel wall [7]. The choice of coil length, shape and stiffness is currently based largely on the experience of the medical professional, and it often remains unclear which configuration provides the most favourable conditions for healing (or even if an alternative treatment method should be preferred) [25]. Therefore, it is of utmost importance to gain better understanding of the hemodynamics after coil insertion through numerical flow simulations, allowing the effects of different coil designs to be assessed a priori.

The first approach to study the flow in these kind of media is the direct computation of flow problems (e.g. the associated Stokes or Navier–Stokes problems). However, simulating the flow in a multiscale medium with many obstacles is very challenging. Typically, resolving such fine structures with mesh-based solvers results either in poor element quality or high computational cost, due to the large element number needed to resolve the device sufficiently. In order to overcome these difficulties, a popular class of numerical methods has been developed in the literature, which is based on the strategy of averaging or “upscaling”, i.e. it approximates microscale models by macroscopic models which incorporate local informations about the unresolved microscale features. Possibly the most popular approach to achieve this is based on Representative Elementary Volumes (REVs) and spatial averaging [18]. The idea of this approach can be summarised as follows, see e.g. [14]. Let u be a real-valued function on a domain Ω which describes certain physical quantities with rapid spatial oscillations. To smoothen this function, one considers local averages in a small neighbourhood $V(x)$ about the point x representative for the material — the (local) REV. If the oscillations of u reflect the behaviour of the physical quantity in question on a “microscale”, the averaged function $\langle u \rangle$ is assumed to describe its properties on the (much larger) observation scale, i.e. on the “macroscale”. Mathematical homogenisation is another method allowing to “upscale” differential equations [14]. While the ratio of characteristic microscopic length and characteristic macroscopic length, $\varepsilon > 0$, is a small number determined by the geometry of the problem, the idea of homogenisation is to consider a family of functions $(u_\varepsilon)_\varepsilon$ and to determine the limit

$$(1) \quad u = \lim_{\varepsilon \rightarrow 0} u_\varepsilon.$$

This limit is then considered the upscaled unknown and the objective of the homogenisation procedure is to determine the system of (differential) equations satisfied by the limit u and proving that (1) in fact holds. In this context, for flow problems, the well-known Darcy law, first introduced empirically by [10], plays an important role, by giving a relation between the flow and the characteristics of the porous medium via the permeability tensor \mathbf{K} , i.e.

$$v = \frac{1}{\mu} \mathbf{K}(f - \nabla p),$$

where v is the Darcy velocity, p the pressure, f an external force and $\mu > 0$ is the viscosity. As a result of periodic homogenisation, the entries of the permeability tensor \mathbf{K} are given by certain averages over the periodicity cells involving the solutions to auxiliary flow problems stated on the periodicity cell. Analytical expressions for the permeabilities for an arrangement of cylinders (representing fibrous media with parallel cylindrical fibres) were derived in [6] using homogenisation in periodic media and the self-consistent method. It has to be noted that the empirical Darcy law does not rely on any periodicity assumption. Nonetheless, in what follows, we give a mathematical justification of the Darcy law in periodic porous media, which allows also to give an explicit formulation for the permeability tensor \mathbf{K} in terms of rotation matrices and transversal and longitudinal permeabilities.

An approach based on rotation matrices and analytical expressions for transversal and longitudinal permeabilities was employed for simulation of blood flow through coiled aneurysms in [20, 21, 15]. However, in these works only the diagonal terms of the permeability matrix \mathbf{K} were considered. The objective of this work is first to assess if the effective permeability can be modelled by certain explicit formulas for the transversal and longitudinal permeabilities, and to what extent the rotational transformation associated with analytical expressions for permeability allows to model effectively the permeability tensor of anisotropic fibre-like microscopic geometries, with a particular emphasis on coiled aneurysms. The validation permeabilities are computed from expressions for the permeability based on solutions to cell problems (potentially with slight modifications, namely oversampling, see below) assuming that the fibre-like anisotropic media exhibit a quasi-periodic behaviour. In Section 2, we propose a numerical validation of the permeability for anisotropic microscopic geometries, and apply it to a realistic coil in Section 3, while in Section 4, we use the modelled permeability matrix \mathbf{K} to compute the flow in complex geometries using the Darcy equation.

2. DERIVATION AND NUMERICAL VALIDATION OF THE PERMEABILITY FOR ANISOTROPIC MICROSCOPIC GEOMETRIES

In this section, we validate tensorial permeabilities resulting from anisotropic microstructures. As test case, we employ a coil packing which is one of the standard medical devices used for cerebral aneurysm treatment.

2.1. Flow in porous media. Consider the Stokes problem in a heterogenous domain Ω_ε . The steady-state Stokes problem in the domain Ω_ε with homogeneous Dirichlet boundary condition is to find the velocity $u_\varepsilon : \Omega_\varepsilon \rightarrow \mathbb{R}^N$ and the pressure $p_\varepsilon : \Omega_\varepsilon \rightarrow \mathbb{R}$, solution to

$$(2) \quad \begin{aligned} -\mu \Delta v_\varepsilon + \nabla p_\varepsilon &= f & \text{in } \Omega_\varepsilon, \\ \nabla \cdot v_\varepsilon &= 0 & \text{in } \Omega_\varepsilon, \\ v_\varepsilon &= 0 & \text{on } \partial\Omega_\varepsilon, \end{aligned}$$

where $\mu > 0$ is the viscosity and f an applied force with the usual regularity. In the literature, some authors consider a different scaling of (2), replacing the velocity v_ε by $v_\varepsilon = \varepsilon^2 v_\varepsilon$; however, this does not change the methodology nor the results, up to an ε^2 factor in certain places. To proceed, let $\Omega \subset \mathbb{R}^N$ be a regular bounded open set divided into a fixed solid part \mathfrak{B}_ε and its complementary fluid part Ω_ε . We denote by (\cdot, \cdot) the usual scalar product in $L^2(\Omega_\varepsilon)$; we use the same notation for vector-valued functions. We introduce the classical velocity space $V = [H_0^1(\Omega_\varepsilon)]^N = \{u \in [H^1(\Omega_\varepsilon)]^N \text{ such that } u|_{\partial\Omega_\varepsilon} = 0\}$ and pressure space $M = L_0^2(\Omega_\varepsilon) = \{q \in L^2(\Omega_\varepsilon) \text{ such that } \int_{\Omega_\varepsilon} q = 0\}$ as well as the bilinear forms $a : V \times V \rightarrow \mathbb{R}$ and $b : M \times V \rightarrow \mathbb{R}$,

$$a(u, v) = \mu(\nabla u, \nabla v), \quad b(p, v) = -(p, \nabla \cdot v).$$

Then, assuming that $f \in [L^2(\Omega)]^N$, a weak formulation of the Stokes problem (2) reads as follows: find $u_\varepsilon \in V$ and $p_\varepsilon \in M$ such that

$$(3) \quad \begin{cases} a(u_\varepsilon, v) + b(p_\varepsilon, v) &= (f, v), & v \in V, \\ b(q, u_\varepsilon) &= 0, & q \in M. \end{cases}$$

It is well-known that if Ω_ε is connected (to ensure that the zero-average condition of the pressure is sufficient to remove the undetermined constant of the pressure) there exists a unique weak solution to (3) [11].

Denoting the unit cell (periodicity cell of unit side length) by $Y = (0, 1)^N$, we assume that the domain Ω is perforated by a periodically arranged set of closed obstacles \mathfrak{B}_ε of size ε , i.e., $\mathfrak{B}_\varepsilon = \Omega \cap \cup_{k \in \mathbb{Z}} \varepsilon(\mathcal{O} + k)$, where \mathcal{O} is the obstacle in the unit cell Y , so that $\Omega_\varepsilon = \Omega \setminus \mathfrak{B}_\varepsilon$. The homogenisation limit of the Stokes equations, i.e. finding the limit system satisfied by the limit of $(u_\varepsilon, p_\varepsilon)$ as ε tends to zero, was first investigated by [22, 27, 2]. A review of these results can be found in [14, 9]. There exists an extension of the solution $(v_\varepsilon, p_\varepsilon)$ of (2) such that the velocity converges weakly in $[L^2(\Omega)]^N$ to v and the pressure converges strongly in $L_0^2(\Omega)$ to p , where (v, p)

is the unique solution to the homogenised (Darcy) problem,

$$(4) \quad \begin{cases} v &= \frac{1}{\mu} \mathbf{K}(f - \nabla p) & \text{in } \Omega, \\ \nabla \cdot v &= 0 & \text{in } \Omega, \\ v \cdot \nu &= 0 & \text{on } \partial\Omega, \end{cases}$$

with ν the outward unit normal vector to $\partial\Omega$. Moreover, the sharp convergence rate $O(\sqrt{\varepsilon})$ for the energy norm of the difference between the Stokes and Darcy velocities was shown in [3]. Defining the cell problems for $i = 1, \dots, N$ by finding $w_i : Y \rightarrow \mathbb{R}^N$ and $\pi_i : Y \rightarrow \mathbb{R}$, Y -periodic and solutions to

$$(5) \quad \begin{cases} -\Delta w_i + \nabla \pi_i &= e_i & \text{in } Y \setminus \mathcal{O}, \\ \nabla \cdot w_i &= 0 & \text{in } Y \setminus \mathcal{O}, \\ w_i &= 0 & \text{in } \mathcal{O}, \end{cases}$$

it follows that the permeability tensor \mathbf{K} is given by

$$(6) \quad \mathbf{K}_{ij} = \frac{1}{|Y|} \int_{Y \setminus \mathcal{O}} \nabla w_i \cdot \nabla w_j \, dy = \frac{1}{|Y|} \int_{Y \setminus \mathcal{O}} w_i \cdot e_j \, dy, \quad 1 \leq i, j \leq N,$$

where the last equality is obtained by integration by parts, and where $(e_j)_j$, $j = 1, \dots, N$, is the canonical basis of \mathbb{R}^N . It has to be noted that such an approach holds beyond the periodic case, for example in the case of perforated domains defined as a local perturbation of the periodically perforated domain, see e.g. [31], or even for non-periodically evolving microstructures [29, 30]. Thus, various engineering applications involving flow through complex porous media require accurate knowledge of the permeability tensor \mathbf{K} . However, the computation of \mathbf{K} is often non-trivial due to the heterogeneous and anisotropic nature of such materials. The modelling of the permeability tensor therefore represents a significant area of research in engineering and geosciences. A common engineering approach is to express \mathbf{K} as a function of the porosity, which is the volume fraction of the fluid phase within the medium. A benchmark and comparison of different methods to estimate the permeability of regular porous structures can be found in [28] from the famous and well-known Kozeny–Carman relation [17, 8] to more advanced approaches such as pore-scale simulations, although limited to a relatively simple geometry, that is circular obstacles in two dimensions and cylinders in three dimensions.

In this present work, motivated by the study of flow in coiled aneurysms which exhibit a fibre-like structure, we pay particular attention to the derivation of the permeabilities of [6]. Indeed, the analytical permeabilities for an arrangement of cylinders (representing fibrous media with parallel cylindrical fibres) were derived in [6] using homogenisation of periodic media and the self-consistent method. Let R be the radius of the cylinders, let ϕ be the porosity (the volume fraction of the fluid phase) of the fibrous medium and let $\rho = 1 - \phi$ (the volume fraction of the solid phase). Using the subscripts \perp and \parallel for the transversal and longitudinal directions, respectively, and the subscripts p and v for the methods based on statically continuous fields and kinematically continuous fields, respectively, it was shown that the transversal and longitudinal permeabilities are given by

$$(7) \quad K_{\perp, p} = -\frac{R}{8\sqrt{\rho}} \left(\log(\rho) + \frac{1 - \rho^2}{1 + \rho^2} \right), \quad K_{\perp, v} = -\frac{R}{8\sqrt{\rho}} \left(\log(\rho) + \frac{2(1 - \rho)}{1 + \rho} \right),$$

and

$$(8) \quad K_{\parallel, p} = -\frac{R^2}{4\rho} \left(\log(\rho) + \frac{(1 - \rho)(3 - \rho)}{2} \right), \quad K_{\parallel, v} = -\frac{R^2}{4\rho} \left(\log(\rho) + \frac{2(1 - \rho)}{1 + \rho} \right).$$

As noted in [6], in case of transverse flow, the gradient is perpendicular to the cylinder axis, and the problem is fully determined in a (r, θ) -plane of zero thickness in parallel direction. Then, the intrinsic permeability is related to a flow per length perpendicular to the pressure gradient in the (r, θ) -plane, instead of a usual flow per area. This is the reason why $K_{\perp, v}$ and $K_{\perp, p}$ in (7) have the dimension of a length instead of a squared length. In order to recover the usual dimension of

the intrinsic permeability, we have to consider a unit length of material in the cylinder direction. However, we may replace this length by an arbitrary length, such as $R/\sqrt{\rho}$, which leads to

$$(9) \quad K'_{\perp,p} = -\frac{R^2}{8\rho} \left(\log(\rho) + \frac{1-\rho^2}{1+\rho^2} \right), \quad K'_{\perp,v} = -\frac{R^2}{8\rho} \left(\log(\rho) + \frac{2(1-\rho)}{1+\rho} \right).$$

Given these dimensional considerations, we henceforth restrict our attention to the permeabilities defined in (8) and (9).

For a given fibre (modelled as a cylinder) within a unit cell, let \mathbf{R}_θ be the rotation matrix which maps the vertical axis e_z to the fibre direction. Now, assuming that the direction given by the angle θ represents the principal direction of the flow, we propose to estimate the permeability tensor as

$$\mathbf{K} = \mathbf{R}_\theta \begin{pmatrix} K_\perp & 0 & 0 \\ 0 & K_\perp & 0 \\ 0 & 0 & K_\parallel \end{pmatrix} \mathbf{R}_\theta^\top,$$

where the superscript \top denotes the transpose, and where we propose to model the permeabilities K_\parallel and K_\perp using (8) and (9).

For the sake of comparison, in this paper, we also consider an isotropic Kozeny–Carman permeability, i.e. $\mathbf{K}_{\text{iso}} = K_{\text{iso}} \mathbf{I}_3$, with \mathbf{I}_3 the identity matrix of \mathbb{R}^3 and K_{iso} given by [24] as (using the same notations as previously)

$$(10) \quad K_{\text{iso}} = \frac{(2R)^2(1-\rho)^3}{150\rho^2}.$$

2.2. Preliminary results. In this section, we introduce some theoretical results linked to scaling and rotation of the unit cell.

Lemma 1. *For any real number $\kappa > 0$, consider a scaled unit cell $Y^\kappa = (0, \kappa)^N$. Introducing the scaled variable $z := \kappa y$, $y \in Y$, the scaled permeability matrix satisfies*

$$\mathbf{K}^\kappa = \kappa^2 \mathbf{K},$$

where \mathbf{K} is given by (6) and \mathbf{K}^κ is defined by the same relation but replacing Y by Y^κ in (5) and (6).

Proof. When computing the homogenised coefficients in the domain Y^κ , one must average over the periodicity cell Y^κ , whose volume is κ^N . Let ω_i^κ denote the cell solution associated with the periodicity cell Y^κ . By introducing the change of variable $z := \kappa y$, $y \in Y$, it follows that the rescaled function satisfies $\omega_i^\kappa(z) = \kappa \omega_i(\frac{z}{\kappa})$, where ω_i denotes the solution to the reference cell problem defined on the unit cell. \square

Remark 2. *The scaling law of Lemma 1 also applies to the next order Stokes cell problems, namely $\gamma_{ij}^\kappa(z) = \kappa^2 \gamma_{ij}(\frac{z}{\kappa})$, $1 \leq i, j \leq N$.*

Lemma 3. *Let $Y = (0, 1)^N$ be the unit cell and \mathcal{O} be a unit cylinder oriented along an axis e_i , $1 \leq i \leq N$, of \mathbb{R}^N . Furthermore, let*

$$\mathfrak{B}_\varepsilon = \bigcup_{k \in \mathbb{Z}^N} \varepsilon(\mathcal{O} + k)$$

be the periodic arrangements of obstacles and let $\mathbf{R}_\theta \in SO(N)$ be a rotation. If and only if there exists a scalar $\lambda > 0$ such that $\lambda \mathbf{R}_\theta \in \mathbb{Z}^{N \times N}$, then there exists an invertible integer matrix $\mathbf{M} \in \mathbb{Z}^{N \times N}$ such that

$$\mathbf{R}_\theta(\mathbb{Z}^N) = \frac{1}{\lambda} \mathbf{M}(\mathbb{Z}^N)$$

and there holds the identity

$$\mathbf{R}_\theta(\mathfrak{B}_\varepsilon) = \bigcup_{\ell \in \frac{1}{\lambda} \mathbf{M}(\mathbb{Z}^N)} \varepsilon(\mathbf{R}_\theta(\mathcal{O}) + \ell).$$

Proof. If $\lambda \mathbf{R}_\theta \in \mathbb{Z}^{N \times N}$ for some $\lambda > 0$, then setting $\mathbf{M} := \lambda \mathbf{R}_\theta$ gives an invertible integer matrix such that

$$\mathbf{R}_\theta(\mathbb{Z}^N) = \frac{1}{\lambda} \mathbf{M}(\mathbb{Z}^N).$$

Consequently, the rotation of the periodic arrangement satisfies

$$\mathbf{R}_\theta(\mathfrak{B}_\varepsilon) = \bigcup_{\ell \in \frac{1}{\lambda} \mathbf{M}(\mathbb{Z}^N)} \varepsilon(\mathbf{R}_\theta(\mathcal{O}) + \ell).$$

Conversely, if such an integer matrix \mathbf{M} exists, then $\lambda \mathbf{R}_\theta = \mathbf{M} \in \mathbb{Z}^{N \times N}$, establishing the equivalence. \square

Remark 4. *Lemma 3 is essentially a lattice preservation property under a rotation of the cylinders and ensures that the unit cell is changed by a single uniform scaling λ and defines $\frac{1}{\lambda} \mathbf{M}(\mathbb{Z}^N)$ as the new lattice. Intuitively, this condition restricts \mathbf{R}_θ to “rational rotations” that map the integer lattice \mathbb{Z}^N onto a scaled copy of itself, ensuring the periodic structure is preserved. For the rotation of an angle θ in a two-dimensional plane, this condition is equivalent to the existence of a $\lambda > 0$ such that $\lambda \cos(\theta)$ and $\lambda \sin(\theta) \in \mathbb{Z}$. So all angles θ satisfying this condition are exactly those for which $\tan(\theta)$ is a rational number. For example, with $\theta = \frac{\pi}{4}$ with $\lambda = \sqrt{2}$ gives*

$$\lambda \mathbf{R}_{\pi/4} = \sqrt{2} \begin{pmatrix} \frac{1}{\sqrt{2}} & -\frac{1}{\sqrt{2}} \\ \frac{1}{\sqrt{2}} & \frac{1}{\sqrt{2}} \end{pmatrix} = \begin{pmatrix} 1 & -1 \\ 1 & 1 \end{pmatrix} \in \mathbb{Z}^{2 \times 2}.$$

From (6), it follows that the tensor \mathbf{K} is symmetric and positive semi-definite. Consequently, there exists an orthogonal matrix \mathbf{O} and a diagonal tensor \mathbf{K}_{eff} , such that

$$(11) \quad \mathbf{K} = \mathbf{O} \mathbf{K}_{\text{eff}} \mathbf{O}^\top.$$

\mathbf{K}_{eff} is called the effective permeability tensor. In the following lemma, we give a characterisation of the matrix \mathbf{O} for a particular case.

Lemma 5. *Let \mathbf{R}_θ be a rotation satisfying Lemma 3, i.e. there exists a scalar $\lambda > 0$ such that $\lambda \mathbf{R}_\theta \in \mathbb{Z}^{N \times N}$, and consider the rotated variable $z := \mathbf{R}_\theta y$. Let us consider an inclined fibre $\tilde{\mathcal{O}}$ inside the unit cell Y , i.e. $\tilde{\mathcal{O}} = \mathbf{R}_\theta(\mathcal{O})$, where \mathcal{O} is the reference fibre oriented along the vertical axis e_N . Then, there exists a diagonal tensor \mathbf{K}_{eff} such that*

$$(12) \quad \mathbf{K} = \mathbf{R}_\theta \mathbf{K}_{\text{eff}} \mathbf{R}_\theta^\top,$$

that is $\mathbf{O} = \mathbf{R}_\theta$, where the matrix \mathbf{O} is defined in (11).

Proof. Equation (12) follows directly from the classical transformation of the cell problems (5) under scaling and rotation. \square

Remark 6. *Although (12) is strictly valid only for certain rotation angles due to Lemma 3, numerical experiments indicate that it remains a reliable, albeit approximate, description even for angles which break the cell symmetry. Up to a reordering of the eigenvalues of \mathbf{K}_{eff} , the effective permeability tensor can be identified with a scaled version of the reference permeability \mathbf{K}_0 , where \mathbf{K}_0 corresponds to the case in which the fibres are aligned with the vertical axis.*

2.3. Numerical validation of the permeabilities. This section has two main objectives. The first is to validate the analytical expressions for the permeabilities (8) and (9) using numerical experiments. The second objective is motivated by the study of the actual coil geometry, in which the coil within the REVs, namely the unit cell, do not align on opposite faces of the unit cube, preventing the use of periodic boundary conditions. To address this, we embed the REV within a larger computational cell (oversampling), enabling the application of periodic boundary conditions. Consequently, we propose a calibration procedure to determine the true permeability corresponding to the oversampled configuration.

First, to validate the analytical expressions for the permeabilities (8) and (9), we consider arrangements within a unit cell Y consisting of 1 to 16 cylinders of radius $R = 0.1$, all oriented along the e_z -axis. For each specified number of cylinders (from 1 to 16), 10 random arrangements

are generated, with a minimum distance of 0.04 enforced between cylinders. For each configuration, the analytical permeabilities (8) and (9) are compared with the entries of the permeability tensor (6). To this end, the cell problems (5) are solved using the Finite Element method with a Taylor–Hood $\mathbb{P}_2\text{--}\mathbb{P}_1$ discretization on a mesh sufficiently fine to resolve the geometry. The computations are carried out in FreeFEM (a finite element software) [12], and the permeability tensor is then obtained using (6). The resulting permeability matrix \mathbf{K}_{eff} is quasi-diagonal, with off-diagonal terms negligible relative to the diagonal components, i.e. a tensor of the form

$$\mathbf{K} \approx \mathbf{K}_{\text{eff}} \approx \begin{pmatrix} K_{\perp,\text{exp}} & 0 & 0 \\ 0 & K_{\perp,\text{exp}} & 0 \\ 0 & 0 & K_{\parallel,\text{exp}} \end{pmatrix},$$

where, as previously, the subscripts \perp and \parallel denote the transversal and longitudinal permeability, respectively. The subscript “exp” denotes the experimentally obtained permeabilities, emphasising their numerical (as opposed to analytical) aspect. The resulting effective permeabilities are presented in Figure 1. From Figure 1, we observe that the experimental permeabilities are well approximated by the analytical expressions (8) and (9) in general, with minor deviations in the longitudinal permeability for this specific case, for which the one based on statically continuous fields is closer to the experimental permeabilities compared to ones based on kinematically continuous fields or isotropy, both of which almost coincide for all values of porosity.

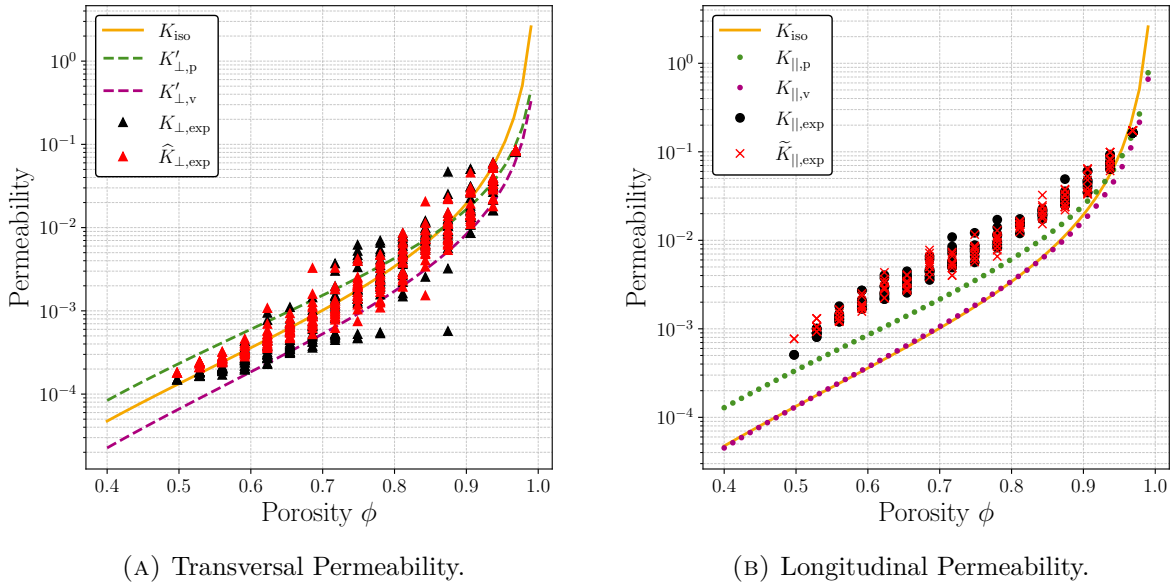


FIGURE 1. Comparisons between computed permeabilities and analytical permeabilities (8), (9) and (10) for arrangements of cylinders of radius $R = 0.1$.

Second, as explained previously, to investigate the actual coil geometry (see Section 3), where the obstacles within the REV do not align on the opposite faces of the unit cube, thus preventing the use of periodic boundary conditions, we embed the REV within a larger computational cell to enable their application. We then propose a procedure to establish the relationship between the true permeability and that obtained from the oversampled configuration. To find this relation, we consider also the same kind of unit cell as previously (i.e. arrangements of cylinders of length 1 and radius $R = 0.1$) but now embedded in a larger cell of size $\kappa = 1.1$, denoted by Y^κ . In this configuration, to compute the permeability tensor \mathbf{K}^κ , we solve the cell problems (5) in the cell Y^κ and compute the permeability as

$$(13) \quad \mathbf{K}_{ij}^\kappa = \frac{1}{|Y^\kappa|} \int_{Y^\kappa} w_i \cdot e_j \, dy, \quad 1 \leq i, j \leq N.$$

The resulting permeability matrix is thus of the form

$$\mathbf{K}^\kappa \approx \mathbf{K}_{\text{eff}}^\kappa \approx \begin{pmatrix} K_{\perp,\text{exp}}^\kappa & 0 & 0 \\ 0 & K_{\perp,\text{exp}}^\kappa & 0 \\ 0 & 0 & K_{\parallel,\text{exp}}^\kappa \end{pmatrix}.$$

At this stage, motivated by [Lemma 1](#), the objective is to find a relation between $\mathbf{K}_{\text{eff}}^\kappa$ and \mathbf{K}_{eff} (the true permeability in the unit cell). As shown by the numerical experiments in [Figure 1](#), we observe that

$$(14) \quad \widehat{K}_{\perp,\text{exp}} \approx \frac{\phi^2}{\kappa^2} K_{\perp,\text{exp}}^\kappa, \quad \widetilde{K}_{\parallel,\text{exp}} \approx \frac{\phi}{\kappa^2} K_{\parallel,\text{exp}}^\kappa,$$

in which the factor κ^2 is motivated by [Lemma 1](#), and ϕ is the porosity (taken in the unit cell). This scaling can be explained by the fact that the relative influence of oversampling is more important in the transversal direction (we add void upstream and downstream of the cylinder direction, which was not originally present). Besides, it is important to note that we are not exactly in the case of [Lemma 1](#), in which the obstacles are also scaled by κ .

We also compute the permeability in a unit cell with a cylinder of different radii, oriented along the e_z -axis. We perform the same computation in the oversampled unit cell, i.e. we consider the previous unit cell but now embedded in a larger cell of size $\kappa = 1.1$. The results are presented in [Figure 2](#). For this test case with only one cylinder, it appears that the right scaling is now (see [Figure 2](#))

$$(15) \quad \widetilde{K}_{\perp,\text{exp}} \approx \frac{\phi}{\kappa^2} K_{\perp,\text{exp}}^\kappa, \quad \widetilde{K}_{\parallel,\text{exp}} \approx \frac{\phi}{\kappa^2} K_{\parallel,\text{exp}}^\kappa.$$

We can thus see that the longitudinal permeability exhibits the same scaling in (14) and (15), while the scaling of the transversal permeability differs slightly. Since the configuration described by (14) more closely reflects the coil arrangement within the REV's (multiple fibres), we adopt the scaling of (14) in [Section 3](#).

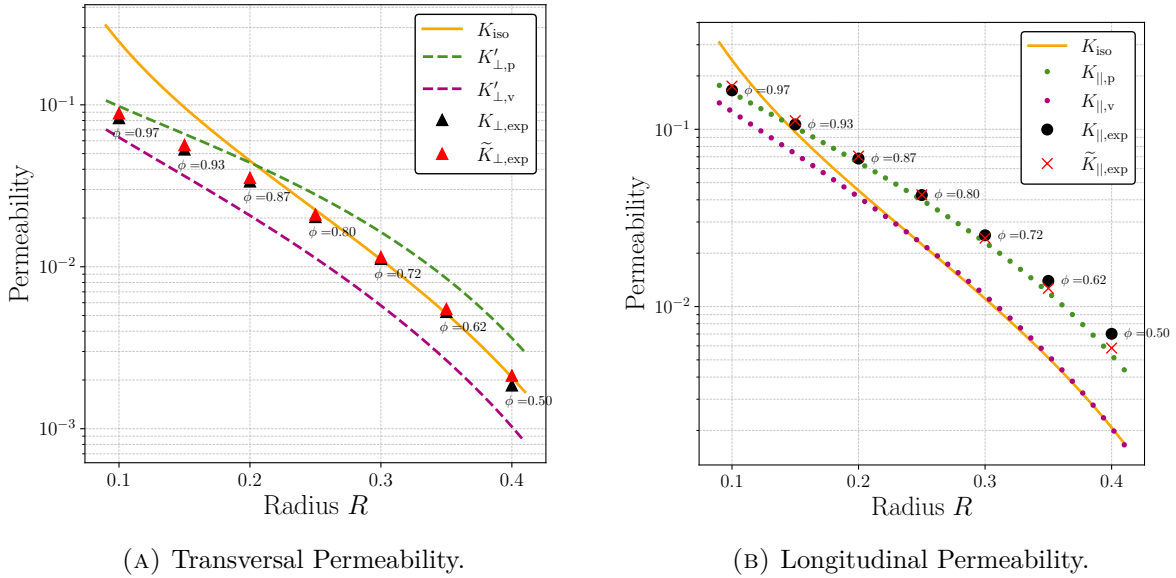


FIGURE 2. Comparisons of permeabilities for one cylinder of different radii.

Lastly, we validate [Lemma 5](#) numerically. To this end, we compute the permeability, using (6), in a new unit cell (of unit side length) obtained by rotation of the whole periodic pattern by an angle θ (which is “rational” in the sense of [Remark 4](#)) about the e_z -axis (note that we use different cylinder radii for the different cases for ease of generation of the unit cell). As result, we obtain a semi-definite positive permeability matrix \mathbf{K} , which we diagonalise as $\mathbf{K} = \mathbf{O} \mathbf{K}_{\text{eff}} \mathbf{O}^\top$, with \mathbf{O} an orthogonal matrix. The objective is now to compare the obtained matrix \mathbf{O} with the theoretical rotation matrix of the angle θ about the e_z -axis, denoted by \mathbf{R}_θ . Numerically, we

find that \mathbf{O} is of the form $\begin{pmatrix} 0 & -c & s \\ 0 & s & c \\ 1 & 0 & 0 \end{pmatrix}$. The idea is now to compare c and s with $\cos(\theta)$ and $\sin(\theta)$, respectively. The results are presented in [Table 1](#).

TABLE 1. Validation of [Lemma 5](#) for different “rational rotations”.

Angle of rotation θ	Experimental values		Theoretical values	
	c	s	$\cos(\theta)$	$\sin(\theta)$
$\arctan(1)$	0.707	0.707	$1/\sqrt{2} \approx 0.707$	$1/\sqrt{2} \approx 0.707$
$\arctan(\frac{4}{5})$	0.780	0.624	$5/\sqrt{41} \approx 0.780$	$4/\sqrt{41} \approx 0.624$
$\arctan(\frac{3}{4})$	0.800	0.599	$4/5 = 0.8$	$3/5 = 0.6$
$\arctan(\frac{1}{2})$	0.894	0.447	$2/\sqrt{5} \approx 0.894$	$1/\sqrt{5} \approx 0.447$
$\arctan(\frac{1}{4})$	0.970	0.242	$4/\sqrt{17} \approx 0.970$	$1/\sqrt{17} \approx 0.242$
$\arctan(\frac{1}{5})$	0.980	0.196	$5/\sqrt{26} \approx 0.980$	$1/\sqrt{26} \approx 0.196$

After validating the analytical expressions for the permeabilities and calibrating the oversampling approach, the next section focuses on the actual geometry of a coil inside an aneurysm. In this context, we employ the relation [\(14\)](#) to determine the true permeability from the oversampled configuration.

3. APPLICATION TO A COIL IN AN ANEURYSM

In this section, we investigate the permeability of a coil packing. To this end, we compute the permeability of several REVs using homogenisation theory and compare the results with the analytical permeability expressions given in [\(8\)](#) and [\(9\)](#). The goal is to assess whether the permeability of the coil packing can be accurately described by these analytical models. In the present work, as benchmark example, we consider the coil presented in [Figure 3](#). It was generated using a mechanical simulation of the insertion process in a cerebral aneurysm, as described in [\[13\]](#). In the simulation, we first insert a stiffer framing coil which provides structural stability. Subsequently, a soft filling coil is inserted into the cage formed by the framing coil, to increase packing density, which often correlates to better occlusion of the aneurysm. The parameters of the inserted coils can be found in [Table 2](#) and closely correspond to those of coils commonly used in practise. With these parameters, we reach a packing density of approximately 30% in the aneurysm.

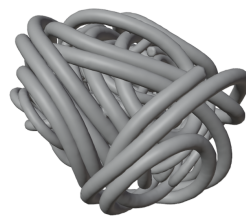
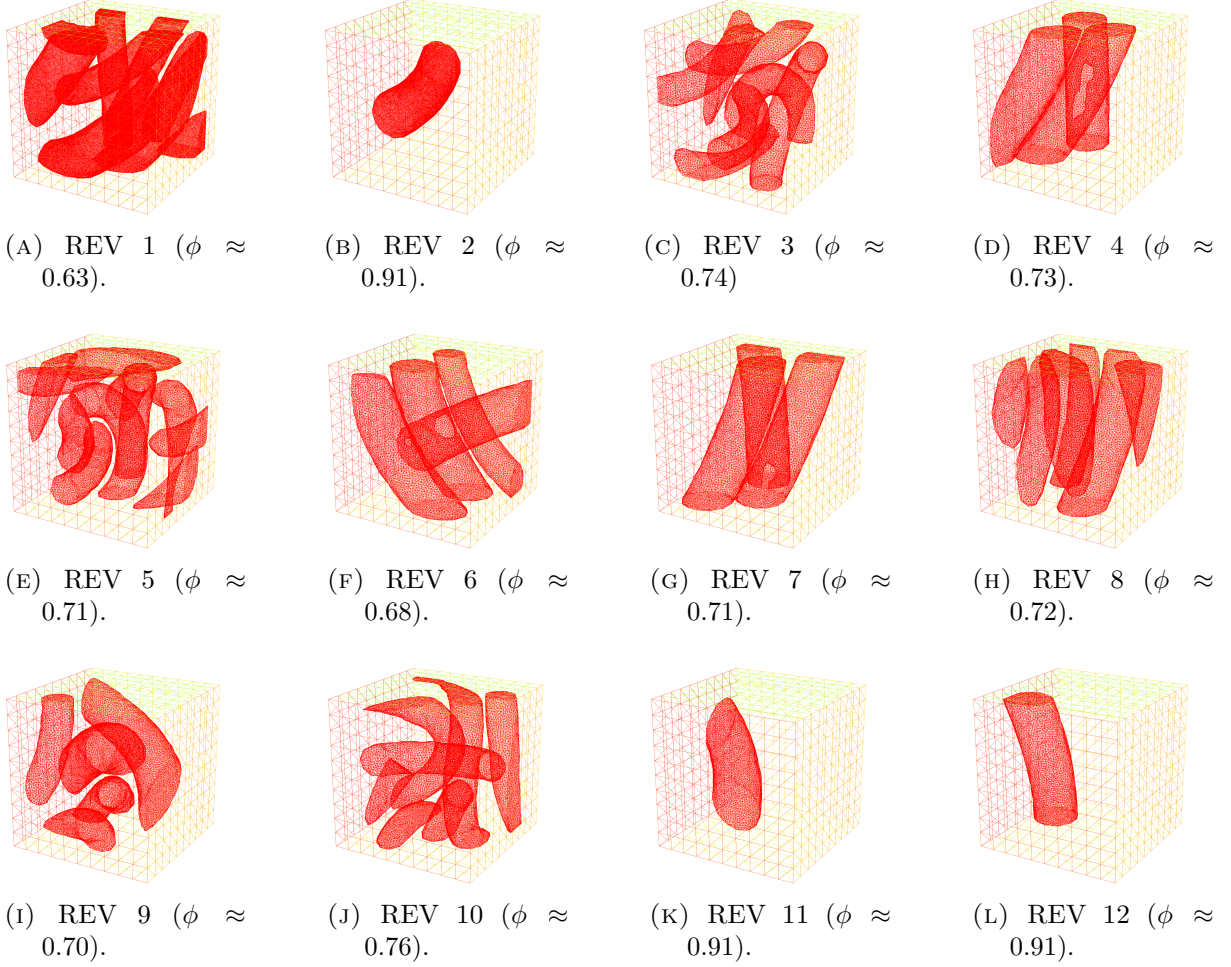


FIGURE 3. The coil under study.

At this stage, the idea is to select several REV within the coil of [Figure 3](#). In this work, the coil is provided as a surface mesh in `.obj` format with quadrilateral elements. Our goal is to extract multiple REV and generate corresponding volume meshes in a format compatible with FreeFEM (the finite element software used for the permeability computation), namely the `.mesh` (Medit) format. The main steps of the REV generation process are summarised in [Algorithm 1](#) (see Appendix). From the coil geometry shown in [Figure 3](#), we select 12 REV of unit size. Some REV are located near the boundary of the coil packing, where the porosity is high, while others

TABLE 2. Parameters of the framing and filling coils.

Parameter	Unit	Framing Coil	Filling Coil
Insertion velocity	[mm/s]	30	30
Internal wire radius	[mm]	0.0381	0.025
Coil radius R_{coil}	[mm]	0.1778	0.127
Coil length	[mm]	150	200
Tertiary coil diameter D	[mm]	4.6	1.75
Shape (in D)	—	Complex	Complex

FIGURE 4. The 12 chosen REV and their respective porosities ϕ .

are taken from the interior regions, characterised by low porosity. The resulting REV obtained using this methodology are shown in [Figure 4](#).

For each REV, we compute the cell problems (5) in the cell Y^κ (we recall that the applications of the periodic boundary conditions are made possible using the oversampled cell Y^κ , with $\kappa = 1.1$ in this work), and compute the permeability using (13). As a result, we obtain a semi-definite positive permeability matrix, $\mathbf{K}_{\text{coil}}^\kappa$, which we diagonalise to find the effective permeabilities, i.e.

$$(16) \quad \mathbf{K}_{\text{coil}}^\kappa = \mathbf{O} \mathbf{K}_{\text{eff,coil}}^\kappa \mathbf{O}^\top$$

with \mathbf{O} an orthogonal matrix and

$$\mathbf{K}_{\text{eff,coil}}^\kappa = \begin{pmatrix} K_{1,\text{coil}}^\kappa & 0 & 0 \\ 0 & K_{2,\text{coil}}^\kappa & 0 \\ 0 & 0 & K_{3,\text{coil}}^\kappa \end{pmatrix}$$

in which $0 < K_{1,\text{coil}}^\kappa \leq K_{2,\text{coil}}^\kappa \leq K_{3,\text{coil}}^\kappa$. Given this ordering, the two smaller effective permeabilities are assumed to be transversal permeabilities and the largest one is assumed to be the longitudinal permeability. Then, to recover the true permeabilities, we apply the scaling (14), i.e.

$$\widehat{K}_{1,\text{coil}} \approx \frac{\phi^2}{\kappa^2} K_{1,\text{coil}}^\kappa, \quad \widehat{K}_{2,\text{coil}} \approx \frac{\phi^2}{\kappa^2} K_{2,\text{coil}}^\kappa, \quad \widetilde{K}_{3,\text{coil}} \approx \frac{\phi}{\kappa^2} K_{3,\text{coil}}^\kappa,$$

where as previously, ϕ is the porosity in the unit cell.

In addition, for the REVs corresponding to coil packings located near the aneurysm wall, we compute the permeability using the same procedure as before, but imposing homogeneous Dirichlet boundary conditions on two opposite faces instead of periodic ones in order to account for wall effects. Periodic boundary conditions are kept on the remaining faces. After applying the same scaling procedure, two effective permeabilities are obtained, denoted $\widehat{K}_{1,\text{coil,Diri-Diri}}$ and $\widehat{K}_{2,\text{coil,Diri-Diri}}$ (the third one is null). We also repeat the computation with homogeneous Dirichlet conditions on one face (corresponding to the wall) and a free outlet on the opposite face, leading to two additional effective permeabilities, $\widehat{K}_{1,\text{coil,Diri-Neu}}$ and $\widehat{K}_{2,\text{coil,Diri-Neu}}$. All corresponding results are presented in Figure 5.

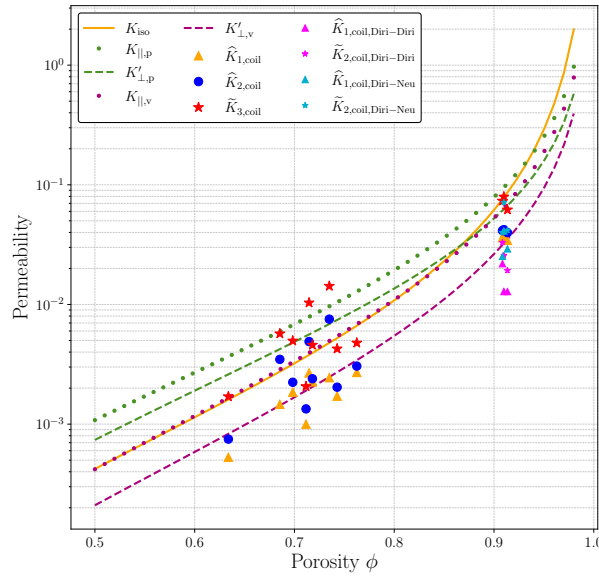


FIGURE 5. Comparison of permeabilities for REVs from the real coil geometry. The analytical permeabilities are computed with $R = R_{\text{coil}} = 0.178$ (Framing Coil).

First, it can be observed that imposing homogeneous Dirichlet boundary conditions reduces the permeability near the wall, effectively accounting for the wall's influence. In the Dirichlet–Neumann case, the permeability decreases by a factor between 1 and 2, and the flow towards the wall is suppressed. From Figure 5, it is obvious that the analytical permeabilities (8) and (9) accurately capture the effective permeabilities of the coil packing, namely $\widehat{K}_{1,\text{coil}}$, $\widehat{K}_{2,\text{coil}}$, $\widehat{K}_{3,\text{coil}}$ and their variants obtained with different boundary conditions on the REVs.

The final step of our analysis consists in assessing whether the relation (12) from Lemma 5 remains valid for the coil REVs, even though the assumptions of the lemma are not satisfied. For each REV in Figure 4, we compute the corresponding rotation matrix \mathbf{R}_θ using Algorithm 4 (see Appendix) which provides the average direction of the coil packing inside the REV. We then compare the computed permeability matrix $\mathbf{K}_{\text{coil}}^\kappa = \mathbf{O} \mathbf{K}_{\text{eff,coil}}^\kappa \mathbf{O}^\top$ defined in (16) to

$$\mathbf{K}_{\text{coil,avg}}^\kappa := \mathbf{R}_\theta \mathbf{K}_{\text{eff,coil}}^\kappa \mathbf{R}_\theta^\top$$

in order to evaluate how accurately the matrix \mathbf{O} can be approximated by \mathbf{R}_θ . To quantify the discrepancy, we use the Frobenius norm, defined as $\|A\|_F = (\sum_{i,j} A_{ij}^2)^{1/2}$, and introduce the

relative error

$$\text{err}_{\mathbf{K}} = \frac{\|\mathbf{K}_{\text{coil}}^{\kappa} - \mathbf{K}_{\text{coil,avg}}^{\kappa}\|_F}{\|\mathbf{K}_{\text{coil}}^{\kappa}\|_F}.$$

The relative errors obtained for all considered REVs are reported in [Table 3](#).

TABLE 3. Comparison of the action of the orthogonal matrix \mathbf{O} of (16) and the action of the rotation matrix \mathbf{R}_{θ} obtained with [Algorithm 4](#) (using a sampling rate $N_s = 40$) for the 12 coil REVs presented in [Figure 4](#).

REV	1	2	3	4	5	6	7	8	9	10	11	12
$\text{err}_{\mathbf{K}}$ [%]	7.2	9.2	10.7	22.0	26.4	20.8	34.2	13.6	17.1	19.0	11.7	12.5

From [Table 3](#), it can be observed that the permeability matrices $\mathbf{K}_{\text{coil}}^{\kappa}$ and $\mathbf{K}_{\text{coil,algo}}^{\kappa}$ are reasonably close. Although the relative error is on average about 20%, this level of discrepancy remains acceptable for our purposes and supports the use of \mathbf{R}_{θ} as a suitable approximation of \mathbf{O} . It should also be noted that the oversampling procedure inevitably results in the loss of certain directional information, which may partly explain this discrepancy.

In the following section, we employ the permeability model established here and evaluate it across various test cases within the framework of the Darcy equation (4).

4. NUMERICAL VALIDATION OF THE UPSCALED MACROSCOPIC MODEL

In this section, we consider three settings of increasing complexity to assess the quality of the effective Darcy flow problem using the permeability parametrisations discussed above. We begin with a cube diagonally cut by cylinders, which is a typical geometry considered in homogenisation, followed by a cylinder cut by spirals, and finally an artificial aneurysm occluded by a coil. All settings contain two main challenges present in most practical applications: the effects of finite size and of boundary conditions. The latter reduce the flow in an aneurysm due to no slip at close-by walls, while the former is due to the fact that the ratio of aneurysm radius to coil radius is quite small (often in the range below 10), which requires caution since direct application of homogenisation results might result in large errors.

In all three settings, the boundary conditions for Darcy flow are $p = 1$ at $x_1 = 0$ and $p = 0$ at $x_1 = L$, where L denotes the length of the domain (in x_1 -direction), and homogeneous Neumann conditions (no flow) at the remaining boundary $\partial\Omega \setminus \{x \in \partial\Omega \text{ such that } x_1 = 0, L\}$. In the first two cases, we compare to the resolved Stokes flow with the corresponding boundary conditions being Neumann conditions $(\nabla v + p\mathbf{I}_3)\nu = \nu$ at $x_1 = 0$ (inflow) and $(\nabla v + p\mathbf{I}_3)\nu = 0$ at $x_1 = L$ (outflow), where ν denotes the outward normal vector, and a homogeneous Dirichlet condition (no-slip) at the remaining boundary $\partial\Omega_{\varepsilon} \setminus \{x \in \partial\Omega_{\varepsilon} : x_1 = 0, L\}$. Then, we compare the resulting average velocities $\bar{v} = |\Omega|^{-1} \int_{\Omega_{\varepsilon}} v_{\varepsilon} dx$ (Stokes) and $\bar{v} = |\Omega|^{-1} \int_{\Omega} v dx$ (Darcy), respectively. Note that we set $\mu = 1$ for simplicity as all problems are linear.

Both the Stokes and Darcy flow problems are discretised using divergence-free discontinuous finite elements of degree $k = 1$. In case of Stokes flow, we use the $\mathbb{BDM}_1\text{-}\mathbb{P}_1$ element with symmetric interior penalty approach with penalty parameter $\alpha = 100$, see e.g. [19] for details. For the Darcy flow problems, we use the mixed discretisation by $\mathbb{RT}_1\text{-}\mathbb{P}_1$ elements. The implementation is done in Python using the FEniCSx library [4].

4.1. Setting 1: Cube cut by cylinders. We consider a cube of side length $L = 1$. The perforated domain Ω_{ε} is constructed from a $4 \times 4 \times 4$ array of identical subdomains, each containing a diagonally oriented cylindrical obstacle \mathcal{O} of radius $R_{\varepsilon} = 1/4$, cf. [Figure 6](#) (left). Hence, the cylinder's length is $L_{\varepsilon} = \sqrt{3}$, leading to a solid fraction of $\rho = \pi R_{\varepsilon}^2 L_{\varepsilon} \approx 0.34$ and a porosity of $\phi = 1 - \rho \approx 0.66$. The effective permeability matrices are obtained using the cylinder

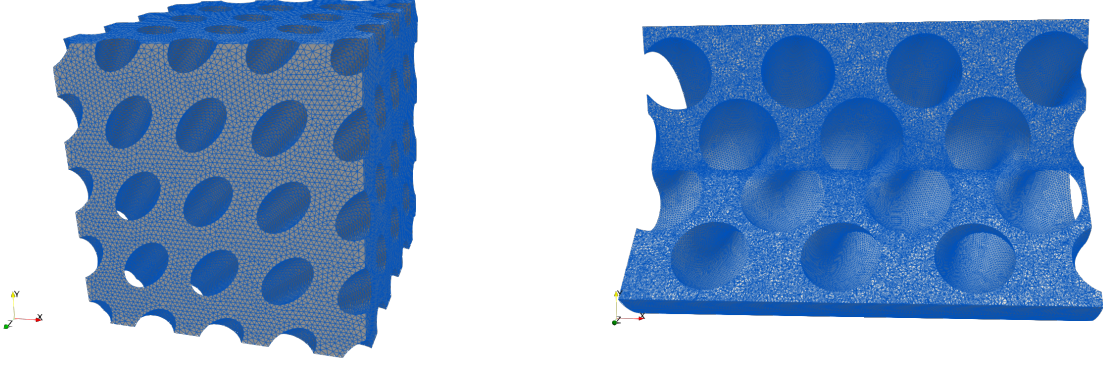


FIGURE 6. Mesh for the Stokes flow simulation of setting 1 (left) and cut through the mesh in setting 2 (right).

TABLE 4. Mesh sizes h , number of mesh elements $|\mathcal{T}_h|$, number of degrees of freedom (DOFs) in velocity and pressure for the Stokes and Darcy flow simulations of the different settings in Section 4.

Setting	Stokes				Darcy			
	h	$ \mathcal{T}_h $	Vel. DOFs	Pr. DOFs	h	$ \mathcal{T}_h $	Vel. DOFs	Pr. DOFs
1) Cube	0.035	711,583	11,001,444	2,364,452	0.03125	196,608	1,787,904	786,432
2) Cylinder	0.035	734,118	11,459,484	2,468,568	0.05	364,710	3,105,465	1,364,480
3) Aneurysm			—		0.15	255,190	2,143,995	939,312

direction $t_c = 3^{-1/2}(1, 1, 1)^\top$ and effective radius $R = \varepsilon R_\varepsilon$ with $\varepsilon = 1/4$:

$$\mathbf{K}_{\text{iso}} = K_{\text{iso}} \mathbf{I}_3 \approx 2.59 \cdot 10^{-4} \mathbf{I}_3,$$

$$\mathbf{K}_p = K_{\parallel,p} t_c \otimes t_c + K'_{\perp,p} (\mathbf{I}_3 - t_c \otimes t_c) \approx 10^{-4} \begin{pmatrix} 4.66 & 0.55 & 0.55 \\ 0.55 & 4.66 & 0.55 \\ 0.55 & 0.55 & 4.66 \end{pmatrix},$$

$$\mathbf{K}_v = K_{\parallel,v} t_c \otimes t_c + K'_{\perp,v} (\mathbf{I}_3 - t_c \otimes t_c) \approx 10^{-4} \begin{pmatrix} 1.79 & 0.45 & 0.45 \\ 0.45 & 1.79 & 0.45 \\ 0.45 & 0.45 & 1.79 \end{pmatrix}.$$

By computing the permeability in the unit cell for this setting (cf. Section 3), we find

$$\mathbf{K}_{\text{hom}}^\varepsilon = \varepsilon^2 \mathbf{K}_{\text{hom}} \approx 5.9 \cdot 10^{-4} t_c \otimes t_c + 2.9 \cdot 10^{-4} (\mathbf{I}_3 - t_c \otimes t_c) \approx 10^{-4} \begin{pmatrix} 3.9 & 0.99 & 0.99 \\ 0.99 & 3.9 & 0.99 \\ 0.99 & 0.99 & 3.9 \end{pmatrix}.$$

Finally, based on the results of Section 2, especially Figure 2, we also consider the weighted average

$$\mathbf{K}_\phi = \frac{3K_{\parallel,p} + K_{\parallel,v}}{4} t_c \otimes t_c + \frac{K'_{\perp,p} + K'_{\perp,v}}{2} (\mathbf{I}_3 - t_c \otimes t_c) \approx 10^{-4} \begin{pmatrix} 3.48 & 0.76 & 0.76 \\ 0.76 & 3.48 & 0.76 \\ 0.76 & 0.76 & 3.48 \end{pmatrix}.$$

The tetrahedral meshes for the Stokes problem are generated using gmsh, while those for the Darcy problems are uniform, see Table 4 for the details. The resulting average velocities are summarised in Table 5 and the diagonal cut through the pressure solutions is depicted in Figure 7. The parametric cases (\mathbf{K}_p and \mathbf{K}_v) significantly over- and under-predict the values (similar to the findings in Section 2). As expected, the isotropic Darcy flow (\mathbf{K}_{iso}) cannot replicate the transversal flow, while the homogenised case ($\mathbf{K}_{\text{hom}}^\varepsilon$) over-predicts the transversal flow. However, the values coincide almost exactly in the averaged case (\mathbf{K}_ϕ). Also, visually, the pressures of the homogenised and averaged cases closely correspond to the Stokes pressure.

TABLE 5. Average velocity components \bar{v}_i ($i = 1, 2, 3$) in setting 1 (cube cut by cylinders) for the Stokes simulation and for the Darcy simulations with different permeability parametrizations \mathbf{K}_\bullet (and the relative deviation from Stokes).

Quantity	Stokes	\mathbf{K}_{iso}	\mathbf{K}_p	\mathbf{K}_v	\mathbf{K}_ϕ	$\mathbf{K}_{\text{hom}}^\varepsilon$
$\bar{v}_1 [\times 10^{-4}]$	3.285	2.588 (-21%)	4.597 (+40%)	1.693 (-48%)	3.333 (+1%)	3.673 (+12%)
$\bar{v}_2 [\times 10^{-4}]$	0.334	0.000 (-100%)	0.262 (-22%)	0.197 (-41%)	0.339 (+2%)	0.435 (+30%)
$\bar{v}_3 [\times 10^{-4}]$	0.334	0.000 (-100%)	0.262 (-21%)	0.197 (-41%)	0.339 (+2%)	0.435 (+30%)

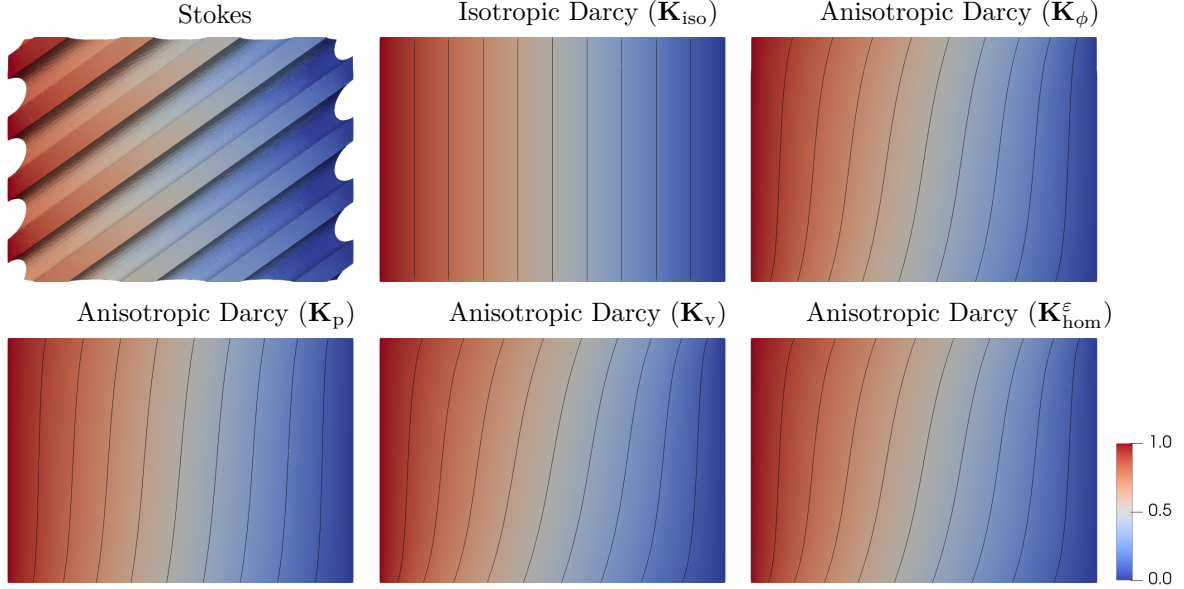


FIGURE 7. Diagonal cut through the pressure solutions (with iso-lines 0.1, 0.2, ..., 0.9) for setting 1 (cube cut by cylinders).

4.2. Setting 2: Cylinder cut by spirals. Next, we consider a domain based on a cylinder of radius one and length $L = 3$ where two spirals are cut out, cf. Figure 6 (right). Both spirals have wire radius $R = 0.25$, and the rotation radii $r_o = 0.65$, $r_i = 0.25$ with 3.5 rotations within the cylinder. The resulting total porosity (w.r.t. the cylinder) is $\phi \approx 0.559$. The tetrahedral meshes for the Stokes and Darcy problems are generated using gmsh, see Table 4 for details.

In a preprocessing step for the calculation of the averaged permeability and porosity, we generate a discretisation of the domain according to Algorithm 2 (see Appendix). First, a structured Cartesian grid is generated with respect to the bounding box of the domain \mathcal{M}_a . From this, a constant spacing Δx is then calculated, depending on the smallest bounding box side length and a sampling rate $N_s = 40$. We then generate mesh nodes in the bounding box, which is extended in length by the REV radius r_{REV} , and centre them around the bounding box by adding $\Delta x/2$. The extension by r_{REV} ensures that each of the nodes contained in \mathcal{M}_a has neighbour points in the box with radius r_{REV} . For the averaging of porosity, we employ Algorithm 3 (see Appendix). We assume that the coil \mathcal{M}_c is fully contained in the aneurysm sack \mathcal{M}_a (the domain to be homogenised), which itself is fully contained in the vessel \mathcal{M}_v . As a first step, we define the volume fraction of fluid and solid $\rho'(x)$ in \mathcal{M} . For each point in the grid, we assign a value $0 \leq \rho_w \leq 1$ if it is contained in the vessel wall, a value of 1 (solid) if it is contained in the coil and a value of 0 (fluid) otherwise. We then average the volume fraction $\rho'(x)$ in the grid points to $\rho(x)$ by either the mean of the grid-points values contained in the box of radius r_{REV} , or by applying a Gaussian filter with a standard deviation of $r_{\text{REV}}/2$. The final porosity is then given by $1 - \rho(x)$ in the points $x \in \mathcal{M} \cap \mathcal{M}_a$. For the averaging of the wire direction, we proceed by Algorithm 4 (see Appendix). We first extract the tangent vector $t_{c,k}$ of

coil k from its centreline. This vector is then transformed into a sign-invariant shape tensor by taking the outer product $t_{c,k} \otimes t_{c,k}$. The shape-tensor field $\mathbf{T}'(x)$ is then defined for each grid point by assigning either the closest shape-tensor field on the spline if the point is within the radius of coil k or zero otherwise. We then average each component of $\mathbf{T}'(x)$ in the same way as in [Algorithm 3](#), by employing a Gaussian of standard deviation of $r_{\text{REV}}/2$ to obtain the averaged field $\mathbf{T}(x)$. By extracting for each grid point the eigenvector of the largest absolute eigenvalue from $\mathbf{T}(x)$, we reconstruct the averaged wire direction.

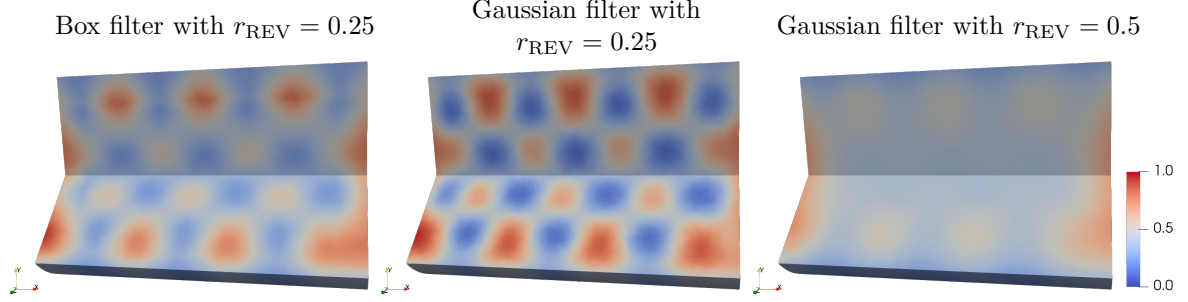


FIGURE 8. Porosity fields of setting 2 generated by [Algorithm 3](#) using $N_s = 40$, $\rho_w = 1$ and different filters.

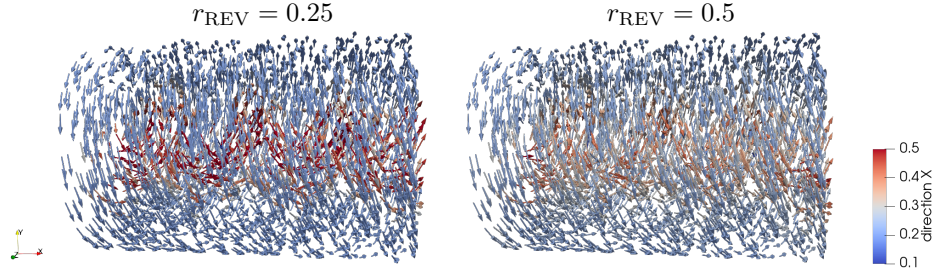


FIGURE 9. Wire-direction fields of setting 2 generated by [Algorithm 4](#) using $N_s = 40$ and different averaging REV radii.

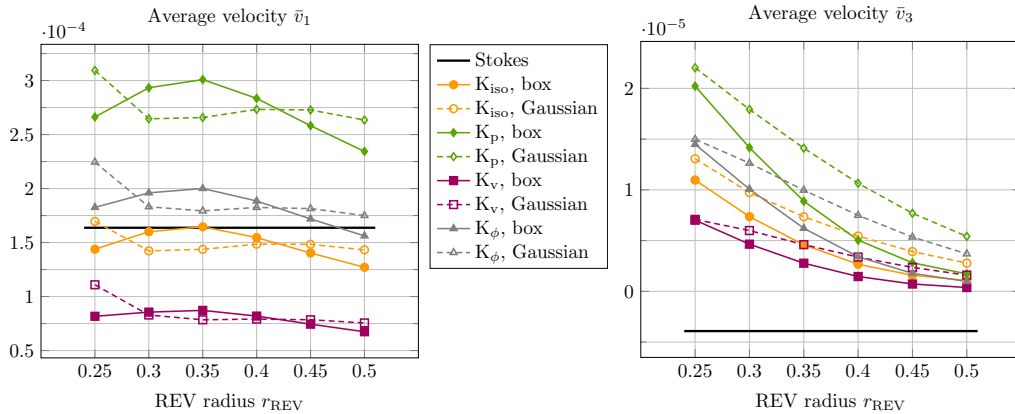


FIGURE 10. Average velocity components \bar{v}_1 (left) and \bar{v}_3 (right) in setting 2 for Stokes and Darcy flow problem (with different permeability parametrisations \mathbf{K}_\bullet and averaging using different filters with $\rho_w = 1$ and $N_s = 40$).

The resulting porosity and wire-direction fields are exemplarily depicted in [Figures 8 and 9](#). With a small averaging radius of $r_{\text{REV}} = 0.25$, i.e. the wire radius of the spirals, microscale details are resolved, while larger averaging radii lead to a more uniform distribution. Likewise, the Gaussian filter yields more pronounced porosity gradients than the box filter. We observed

that the averaging using $\rho_w = 1$, i.e. padding by solid outside the cylinder, yields the best results, while padding by the average porosity $\rho_w = 1 - \bar{\phi}$ or fluid ($\rho_w = 0$) over-predicts the porosity close to the boundary, hence leading to a large Darcy flow along the cylinder wall.

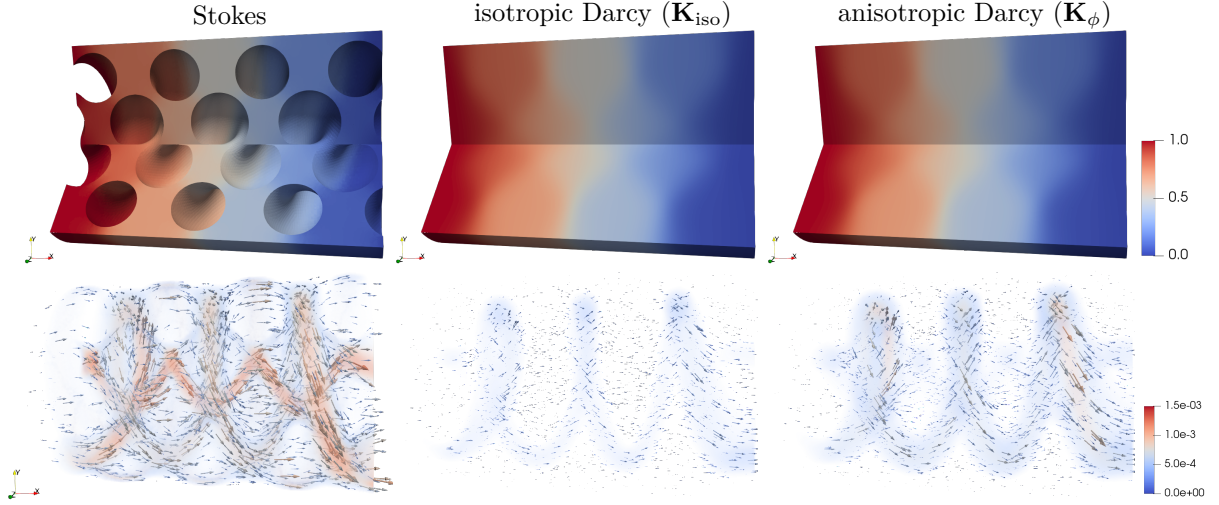


FIGURE 11. Pressure (top line) and velocity (bottom line) solutions for setting 2. For the averaging in the Darcy cases, [Algorithms 3 and 4](#) are used with a Gaussian filter of REV radius of $r_{REV} = 0.35$, $N_s = 40$ and $\rho_w = 1$.

Overall, the effects of the different filters and their REV sizes on the average velocity is minor, as visible in [Figure 10](#) for the average velocity components \bar{v}_1 and \bar{v}_3 , while the average velocity component \bar{v}_2 is always below 10^{-7} . Note that the large deviations in the third component are likely due to the finite-size effects of the Neumann boundary conditions for Stokes flow combined with the boundary layers at in- and out-flow of the averaging (cf. [Figure 8](#)), which decrease for increasing REV radius. As before, the parametric cases (\mathbf{K}_p and \mathbf{K}_v) significantly over- and under-predict the values, while the isotropic (\mathbf{K}_{iso}) and the weighted average (\mathbf{K}_ϕ) cases match quite well. Comparing the pressure and velocity solutions of the Stokes problem and the latter two Darcy cases, as depicted in [Figure 11](#), one observes close correspondence between all pressure fields, but a more localised flow pattern for the anisotropic Darcy case, similar to the Stokes flow.

4.3. Setting 3: Realistic coil in an artificial aneurysm. Finally, we consider an artificial aneurysm occluded by the coil presented in [Figure 3](#), resulting in the geometry depicted in [Figure 12](#) (left). This geometry does not allow for a fully resolved Stokes simulation on a typical computer due to the excessive number of DOFs required for an appropriate three-dimensional mesh. Nevertheless, we can apply the averaging strategy and resolve the Darcy flow. To this end, we apply the averaging [Algorithms 3 and 4](#) (see Appendix) using $N_s = 40$, a Gaussian filter with REV radius $r_{REV} = 0.4$ and solid padding ($\rho_w = 1$), see [Figure 12](#) (right) for the result. For the permeability parametrisation, we choose \mathbf{K}_ϕ based on the previously observed good results, together with $R = 0.1524$, which is the average of the two coil radii. The tetrahedral mesh for the Darcy problem is generated using gmsh, see [Table 4](#) for details. The resulting solution is depicted in [Figure 13](#). The main features of the coil structure are recovered by the porosity field, and thus also the Darcy solution, visible in the heterogeneous pressure field and low velocities in densely packed coil regions.

5. CONCLUSION

This study introduces a comprehensive multiscale framework for determining effective permeabilities in anisotropic microscopic geometries containing dense, fibre-like obstacles, with high relevance to flow prediction in coiled aneurysm. By combining homogenisation theory with simulation in Representative Elementary Volumes, we obtain permeability tensors that capture directional effects imposed by the underlying microstructures. While commonly used isotropic

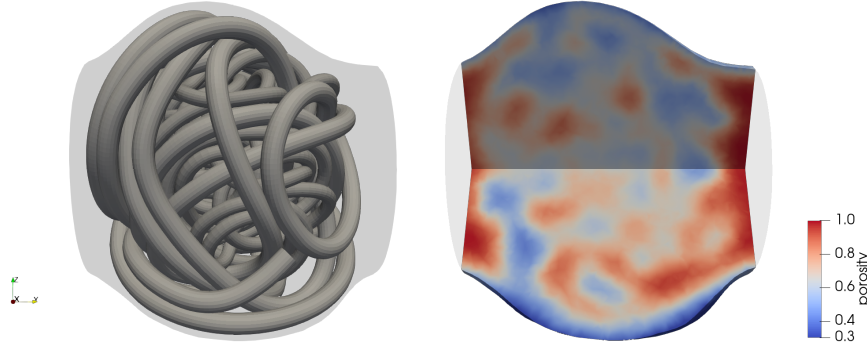


FIGURE 12. Left: Geometry of a coil in an artificial aneurysm. Right: Averaged porosity field generated by Algorithm 3.

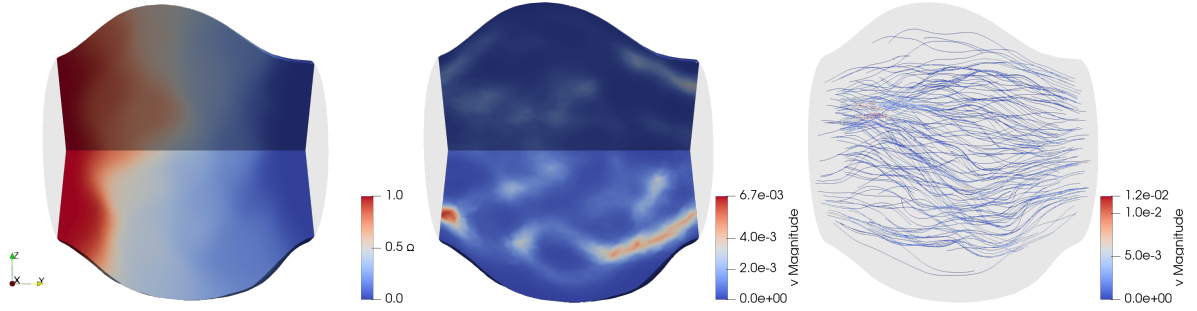


FIGURE 13. Pressure (left), velocity magnitude (centre) and streamlines (right) of the anisotropic Darcy simulation.

models can result in significant inaccuracies, anisotropic permeability tensors can improve macroscopic simulation results significantly. Darcy flow simulations show that anisotropy substantially influences macroscopic flow patterns and pressure distributions. Applying the methodology to a realistic coil geometry further demonstrates its flexibility and predictive capability. Overall, our approach provides a robust pathway for linking microscopic coil arrangements to clinically meaningful flow characterisations, and it offers a flexible foundation which can be extended to other application fields such as fibre-reinforced materials, fractured porous media and biomedical flow configurations.

APPENDIX A. ALGORITHMS FOR HOMOGENIZATION BY SPATIAL AVERAGING

In this sections, we present the Algorithms 1 to 4 employed in this study and cited in the text.

Algorithm 1 Representative Elementary Volumes (REVs) generation

Input: Surface mesh `.obj` of the coil.

 \triangleright *Made of quadrilateral elements.*
Output: Tetrahedral volume mesh of an REV. \triangleright *Readable by a finite element software e.g. FreeFEM.*

- 1: Read the surface mesh `.obj` of the coil with `blender`.
 - 2: Select an REV of size 1 by computing the intersection of the coil with a cube of size 1.
Re-mesh the REV with appropriate mesh size. \triangleright *At this stage, we have a surface mesh (made of quadrilateral elements) of the coil inside a unit cell.*
 - 3: Export the REV in format `.obj`.
 - 4: Open the REV mesh with `meshlab`. Turn the mesh into a pure triangular mesh and re-mesh the coil with appropriate mesh size. Remove spurious components of the mesh and export each component in format `.obj`. \triangleright *Surface mesh made of triangles.*
 - 5: Convert each mesh component `.obj` in a surface mesh `.mesh` using the python plugin `meshio` [23].
 \triangleright *Format `.mesh` readable by FreeFEM.*
 - 6: Import the surface mesh of each component in FreeFEM and glue then together to create a global surface mesh $\mathcal{C}_{h,S}$.
 - 7: Create the surface mesh of the unit box (oversampled with a ratio $\kappa = 1.1$) around the obstacles, denoted $\mathcal{B}_{h,S}$. \triangleright *Ensure that the mesh is compatible with periodic boundary conditions.*
 - 8: Combine $\mathcal{C}_{h,S}$ and $\mathcal{B}_{h,S}$ as $\mathcal{T}_{h,S} = \mathcal{B}_{h,S} \cup \mathcal{C}_{h,S}$.
 - 9: Create the three dimensional volume mesh \mathcal{T}_h (composed of tetrahedra) of $\mathcal{T}_{h,S}$, i.e., filling the space between the bounding box and the coil with tetrahedra, using `TetGen` [26].
-

Algorithm 2 Uniform mesh generation

Input: Aneurysm mesh \mathcal{M}_a ; REV radius $r_{\text{REV}} > 0$; sampling rate $N_s \in \mathbb{N}_+$.

Output: Uniform mesh \mathcal{M} .

- 1: Compute the bounding box centre x_c and length vector L of \mathcal{M}_a
 - 2: $\Delta x = \min\{L_1, L_2, L_3\} / (2N_s)$ \triangleright *mesh spacing*
 - 3: **for all** $i \in \{1, 2, 3\}$ **do**
 - 4: $N_i = \lceil (L_i/2 + r_{\text{REV}}) / \Delta x \rceil$
 - 5: $\mathcal{S}_i = \{x_{c,i} + (n + 1/2)\Delta x \mid n = -N_i, \dots, N_i - 1\}$
 - 6: $\mathcal{M} = \mathcal{S}_1 \times \mathcal{S}_2 \times \mathcal{S}_3$
-

Algorithm 3 Averaging procedure for the porosity field

Input: Coil mesh \mathcal{M}_c , aneurysm mesh \mathcal{M}_a , and vessel mesh \mathcal{M}_v with $\mathcal{M}_c \subseteq \mathcal{M}_a \subseteq \mathcal{M}_v$; wall boundary condition $\rho_w \in [0, 1]$; REV radius r_{REV} ; and uniform mesh \mathcal{M} from [Algorithm 2](#).

Output: Porosity field $\phi(x)$ for $x \in \mathcal{M} \cap \mathcal{M}_a$.

```

1:  $\triangleright$  Initialization and boundary conditions for solid fraction  $\triangleleft$ 
2: for all  $x \in \mathcal{M}$  do
3:    $\rho'(x) = \begin{cases} \rho_w & \text{if } x \in \mathcal{M}_v^c \text{ (wall BC)} \\ 1 & \text{if } x \in \mathcal{M}_c \text{ (coil region)} \\ 0 & \text{otherwise (fluid region)} \end{cases}$ 
4:  $\triangleright$  Apply averaging by convolution over local REV neighborhood (box filter)  $\triangleleft$ 
5: for all  $x \in \mathcal{M} \cap \mathcal{M}_a$  do
6:    $\mathcal{N}(x) = \{x' \in \mathcal{M} \mid \|x - x'\|_\infty \leq r_{\text{REV}}\}$ 
7:    $\rho(x) = \frac{1}{|\mathcal{N}(x)|} \sum_{x' \in \mathcal{N}_{\text{REV}}(x)} \rho'(x')$ 
8:    $\triangleright$  Alternative Gaussian filter with  $\sigma = r_{\text{REV}}/2$ :
       
$$\rho(x) = \left( \sum_{x' \in \mathcal{M}} \rho'(x') \exp\left(-\frac{\|x-x'\|_2^2}{2\sigma^2}\right) \right) / \left( \sum_{x' \in \mathcal{M}} \exp\left(-\frac{\|x-x'\|_2^2}{2\sigma^2}\right) \right)$$
  $\triangleleft$ 
9:    $\phi(x) = 1 - \rho(x)$ 

```

Algorithm 4 Averaging procedure for the direction field

Input: K pairs of coil meshes $\mathcal{M}_{c,k}$ and coil centrelines \mathcal{C}_k , and aneurysm mesh \mathcal{M}_a such that $\mathcal{M}_{c,k} \subseteq \mathcal{M}_a$ for all $k = 1, \dots, K$; REV radius r_{REV} ; and uniform mesh \mathcal{M} from [Algorithm 2](#).

Output: Tangent field $t(x)$ for $x \in \mathcal{M} \cap \mathcal{M}_a$.

```

1:  $\triangleright$  Generate shape tensor field  $\triangleleft$ 
2: for all  $x \in \mathcal{M}$  do
3:    $\mathbf{T}'(x) = \mathbf{0}$ 
4: for  $k = 1, \dots, K$  do
5:   Generate tangent vector  $t_{c,k}(s)$  along the centerline  $s \in \mathcal{C}_k$ 
6:   for all  $x \in \mathcal{M} \cap \mathcal{M}_{c,k}$  do
7:     Find  $s_x = \operatorname{argmin}_{s \in \mathcal{C}_k} \|x - s\|_2$ 
8:      $\mathbf{T}'(x) = t_{c,k}(s_x) \otimes t_{c,k}(s_x)$ 
9:  $\triangleright$  Average shape tensor field  $\triangleleft$ 
10: for all  $x \in \mathcal{M} \cap \mathcal{M}_a$  do
11:   Apply Gaussian-weighted averaging with  $\sigma = r_{\text{REV}}/2$ :
       
$$\mathbf{T}(x) = \left( \sum_{x' \in \mathcal{M}} \exp\left(-\frac{\|x-x'\|_2^2}{2\sigma^2}\right) \mathbf{T}'(x') \right) / \left( \sum_{x' \in \mathcal{M}} \exp\left(-\frac{\|x-x'\|_2^2}{2\sigma^2}\right) \right)$$

12:    $\triangleright$  Extract wire direction  $\triangleleft$ 
13:   Compute normalized eigenvector  $v(x)$  corresponding to the largest absolute eigenvalue of  $\mathbf{T}(x)$ 
14:    $t(x) = v(x)$ 

```


REFERENCES

- [1] A. Adamou, M. Alexandrou, C. Roth, A. Chatziioannou, and P. Papanagiotou. Endovascular treatment of intracranial aneurysms. *Life (Basel, Switzerland)*, 11(4):335, 2021.
- [2] G. Allaire. Homogenization of the Stokes flow in a connected porous medium. *Asympt. Anal.*, 2(3):203–222, 1989.
- [3] L. Balazi, G. Allaire, and P. Omnes. Sharp convergence rates for the homogenization of the Stokes equations in a perforated domain. *Discrete Contin. Dyn. Syst. - Ser. B*, 30(5):1550–1574, 2025.
- [4] I. A. Baratta, J. P. Dean, J. S. Dokken, M. Habera, J. S. Hale, C. N. Richardson, M. E. Rognes, M. W. Scroggs, N. Sime, and G. N. Wells. DOLFINx: the next generation FEniCS problem solving environment. Preprint, 2023.
- [5] J. Bear. *Modeling Phenomena of Flow and Transport in Porous Media*, volume 31 of *Theory and Applications of Transport in Porous Media*. Springer International Publishing, Cham, 2018.
- [6] C. Boutin. Study of permeability by periodic and self-consistent homogenisation. *Eur. J. Mech. A Solids*, 19(4):603–632, 2000.
- [7] W. Brinjikji, D. F. Kallmes, and R. Kadirvel. Mechanisms of healing in coiled intracranial aneurysms: a review of the literature. *Am. J. Neuroradiology*, 36(7):1216–1222, 2015.
- [8] P. C. Carman. Fluid flow through granular beds. *Chem. Eng. Res. Des.*, 75:32–48, 1997.
- [9] G. A. Chechkin, A. L. Piatnitski, and A. S. Shamaev. *Homogenization. Methods and applications*, volume 234 of *Transl. Math. Monogr.* American Mathematical Society (AMS), 2007. Transl. from the Russian by T. Rozhkovskaya.
- [10] H. Darcy. *Les fontaines publiques de la ville de Dijon*. Dalmont, 1856.
- [11] V. Girault and P.-A. Raviart. *Finite element methods for Navier-Stokes equations. Theory and algorithms.*, volume 5 of *Springer Ser. Comput. Math.* Springer, (Extended version of the 1979 publ.) edition, 1986.
- [12] F. Hecht. New development in FreeFem++. *J. Numer. Math.*, 20(3-4):251–265, 2012.
- [13] F. Holzberger, M. Muhr, and B. Wohlmuth. A comprehensive numerical approach to coil placement in cerebral aneurysms: mathematical modeling and in silico occlusion classification. *Biomech. Model. Mechanobiol.*, 23(6):2063–2089, 2024.
- [14] U. Hornung, editor. *Homogenization and Porous Media*, volume 6 of *Interdiscip. Appl. Math.* Springer, 1997.
- [15] M. Horvat, S. B. Lunowa, D. Sytnyk, and B. Wohlmuth. A lattice Boltzmann method for non-Newtonian blood flow in coiled intracranial aneurysms. In *Numerical Mathematics and Advanced Applications ENUMATH 2023*, volume 1, pages 473–483. Springer, 2025.
- [16] J. Hu, H. Albadawi, B. W. Chong, A. R. Deipolyi, R. A. Sheth, A. Khademhosseini, and R. Oklu. Advances in biomaterials and technologies for vascular embolization. *Adv. Mater.*, 31(33):1901071, 2019.
- [17] J. Kozeny. Über die kapillare Leitung des Wassers im Boden. *Sitzungsber. Akad. Wiss. Wien*, 136:271–306, 1927.
- [18] M. Quintard and S. Whitaker. Two-phase flow in heterogeneous porous media: The method of large-scale averaging. *Transp. Porous Med.*, 3(4):357–413, 1988.
- [19] S. Rhebergen and B. S. Southworth. An algebraic preconditioner for the exactly divergence-free discontinuous Galerkin method for Stokes. *Numer. Meth. Part. Diff. Eq.*, 41:e70001, 2025.
- [20] J. Romero Bhathal, F. Chassagne, L. Marsh, M. R. Levitt, C. Geindreau, and A. Aliseda. Modeling flow in cerebral aneurysm after coils embolization treatment: A realistic patient-specific porous Model approach. *Cardiovasc. Eng. Tech.*, 14(1):115–128, 2023.
- [21] J. Romero Bhathal, L. Marsh, M. R. Levitt, C. Geindreau, and A. Aliseda. Towards prediction of blood flow in coiled aneurysms before treatment: A porous media approach. *Ann. Biomed. Eng.*, 51(12):2785–2801, 2023.
- [22] E. Sanchez-Palencia. *Non-homogeneous Media and Vibration Theory*, volume 127 of *Lecture Notes in Physics*. Springer, 1980.
- [23] N. Schlömer. meshio: Tools for mesh files.
- [24] R. Schulz, N. Ray, S. Zech, R. Andreas, and P. Knabner. Beyond Kozeny–Carman: Predicting the permeability in porous media. *Transp. Porous Med.*, 130, 2019.
- [25] B. Seibert, R. P. Tummala, R. Chow, A. Faridar, S. A. Mousavi, and A. A. Divani. Intracranial aneurysms: review of current treatment options and outcomes. *Front. Neurol.*, 2:45, 2011.
- [26] H. Si. TetGen, a Delaunay-based quality tetrahedral mesh generator. *ACM Trans. Math. Softw.*, 41(2), 2015.
- [27] L. Tartar. Convergence of the homogenization process. In *Non-homogeneous Media and Vibration Theory*. Springer, 1980. Appendix of [22].
- [28] A. Wagner, E. Eggenweiler, F. Weinhardt, Z. Trivedi, D. Krach, C. Lohrmann, K. Jain, N. Karadimitriou, C. Bringedal, P. Volland, C. Holm, H. Class, H. Steeb, and I. Rybak. Permeability estimation of regular porous structures: a benchmark for comparison of methods. *Transp. Porous Media*, 138(1):1–23, 2021.
- [29] D. Wiedemann and M. A. Peter. Homogenisation of the Stokes equations for evolving microstructure. *J. Differ. Equations*, 396:172–209, 2024.
- [30] D. Wiedemann and M. A. Peter. A Darcy law with memory by homogenisation for evolving microstructure. *J. Math. Anal. Appl.*, 546:129222, 2025.
- [31] S. Wolf. Homogenization of the Stokes system in a non-periodically perforated domain. *Multiscale Model. Simul.*, 20(1):72–106, 2022.